Supplementary Information:
Geometry-dependent transmission of externally imposed shear stress in confined microtubule-kinesin active fluids

Joshua H. Dickie,[a] Tianxing Weng,[a] Yen-Chen Chen,[a] Haoran Wang,[b] Yutian He,[c] Saloni Saxena,[d,†] Robert A. Pelcovits,[d] Thomas R. Powers,[e,d] and Kun-Ta Wu[a,f,*]

[a] Department of Physics, Worcester Polytechnic Institute, Worcester, Massachusetts 01609, USA
[b] Department of Chemistry and Biochemistry, Worcester Polytechnic Institute, Worcester, Massachusetts 01609, USA
[c] Department of Physics, University of Massachusetts, Amherst, MA 01002, USA
[d] Department of Physics, Brown University, Providence, RI 02912, USA
[e] School of Engineering, Brown University, Providence, RI 02912, USA
[f] The Martin Fisher School of Physics, Brandeis University, Waltham, Massachusetts 02454, USA
[†]Present address: Department of Neuroscience, University of Pittsburg, Pittsburg PA 15260
[*]Corresponding: kwu@wpi.edu

Table of Contents

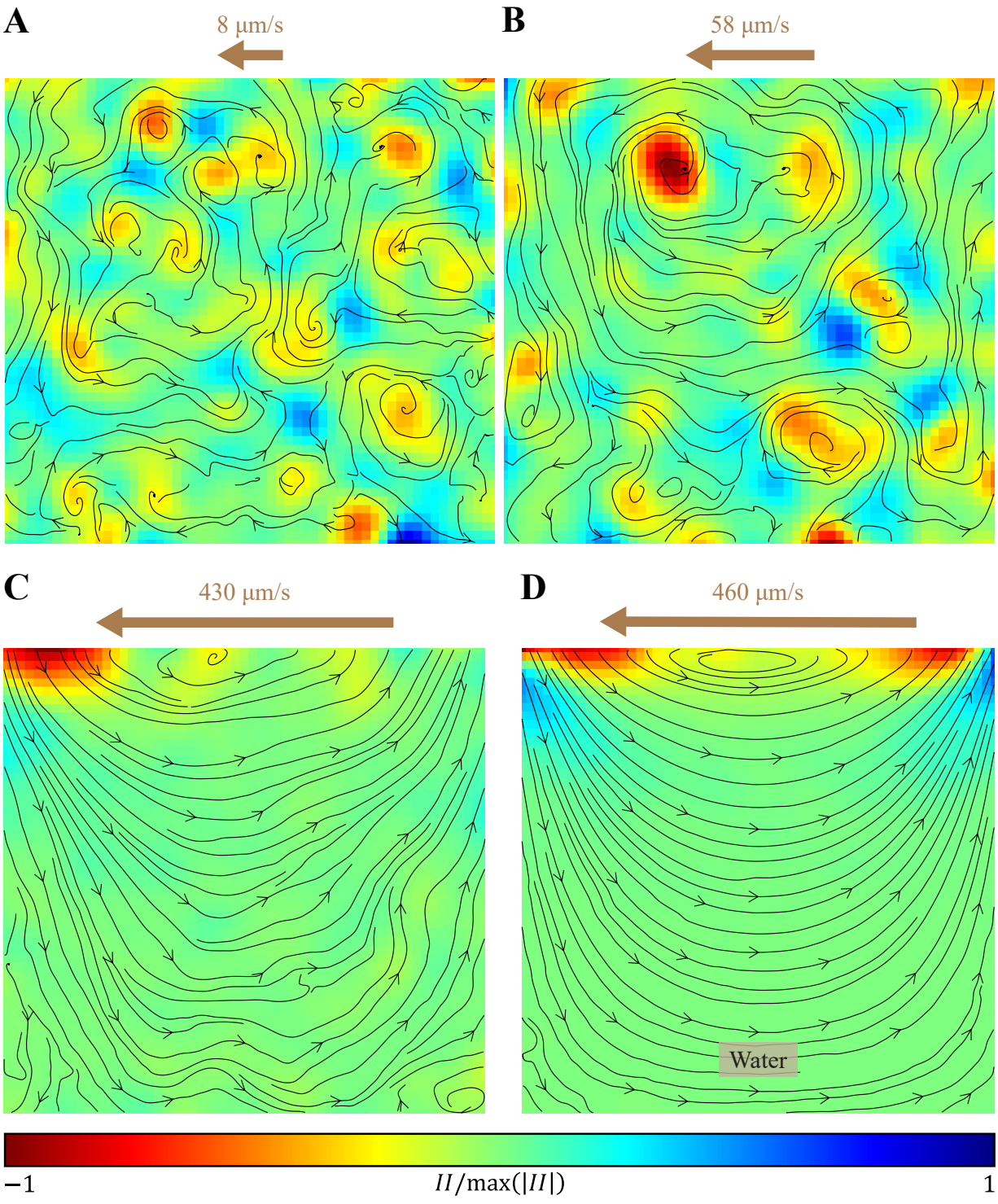

Fig. S1: Normalized Okubo-Weiss field colormap ($II/\max(|II|)$) overlaid with streamlines of fluid flow. The colormap ranges from -1 (red) to $+1$ (blue), where negative values highlight vorticity-dominated regions and positive values indicate strain-dominated regions.[1–3] Panels A–C show the streamline patterns and normalized Okubo-Weiss field for active fluid systems with different thread speeds, while panel D depicts the corresponding results for heavy water. The maps shown are limited to regions $\geq$150 μm away from boundaries to ensure reliable particle tracking and statistics (see Materials and Methods).

Section S1: Effect of shear stress on a fuel-deprived inactive gel

In the absence of ATP, the kinesin motors act as immobile crosslinkers, transforming the microtubule network into an elastic gel (fuel-deprived inactive gel).[4,5] To investigate how this inactive gel responds to shear stress, we examined its flow behavior under varying thread speeds (Movie S3). At low thread speeds (<120 μm/s), the network remained stationary with only minor jiggling and vibration, exhibiting as an elastic gel resisting deformation (Fig. S2A, green dots). As the thread speed exceeded 120 μm/s, the network near the moving boundary fluidized, causing a gradual increase in mean speed. However, even at the highest thread speed, the fuel-deprived inactive gel did not fully fluidize; the bottom half remained elastic-like, resulting in a lower mean speed than water at the same thread speed (Fig. S2A).

To quantify this shear-induced fluidization, we analyzed the shear moving fraction, by first averaging each flow speed on the grid over driving periods and then counting the fraction of grid points where the time-averaged speed exceeded 0.2 μm/s. This fraction represents the proportion of the fluid that was actively moving in response to the shear stress. In active fluid and water/heavy water mixtures, this fraction was 100%, but in the fuel-deprived inactive gel, the shear moving fraction increased with thread speed, showing a transition from a stationary state to partial fluidization (Fig. S2B). These findings highlight that shear stress alone can only partially fluidize an inactive microtubule-kinesin gel. Complete fluidization requires ATP-fueled motors acting as mobile crosslinkers, enabling fluid-like behavior,[6] while simultaneously generating active stress that continuously drives network reorganization.[7]

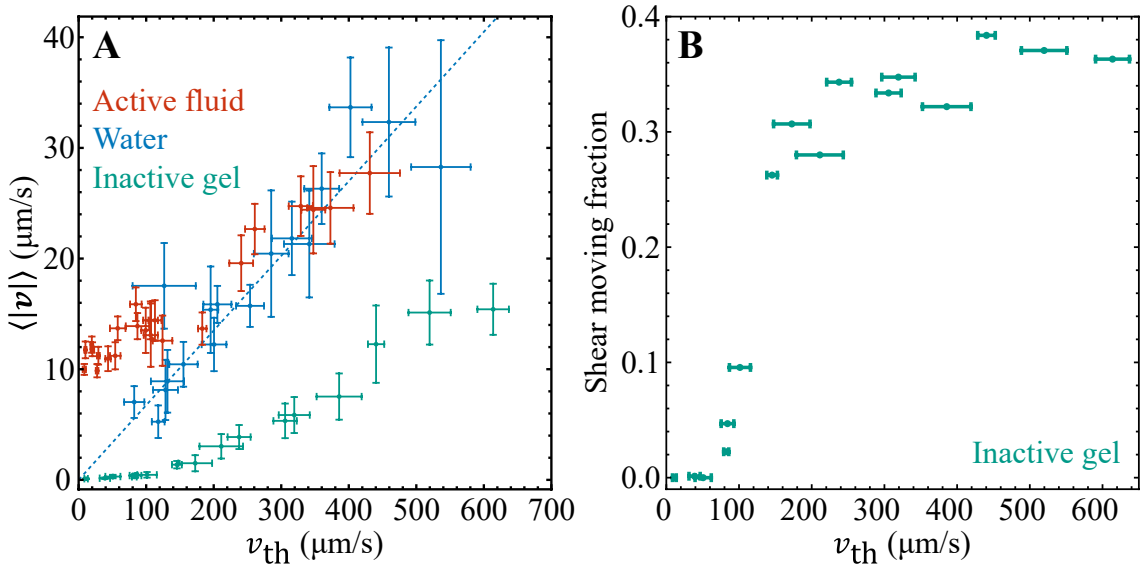

Fig. S2: Shear-induced fluidization of fuel-deprived inactive gel. (A) Mean tracer speed as a function of thread speed v_{th} for active fluid (red dots), water (blue dots), and ATP-free inactive gel (green dots). Error bars represent one standard deviation of temporal variation, with each dot representing an independent experiment. The dashed blue line is a linear fit for water, as shown in Fig. 2A. The active fluid (red) maintained a nearly constant mean speed (~10 μm/s) at low thread speeds (≲120 μm/s), while the inactive gel (green) remained nearly stationary due to its crosslinked viscoelastic network. Only when v_{th} exceeded ~120 μm/s did the inactive gel begin to fluidize, gradually increasing its speed. (B) Shear-induced fluidized fraction of the inactive gel vs. thread speed v_{th}. Unlike active fluid and water, which remained fully fluidized across the thread speeds explored, the inactive gel exhibited a transition from a stationary state (zero shear moving fraction) to partial fluidization (shear moving fraction ≈ 0.4) as v_{th} increased.

Section S2: Estimation of the critical shear stress at the kinematic transition

Our simulations have shown that the transition from active stress–dominated dynamics to external shear stress–dominated dynamics occurs when viscous stress is comparable to the internal active stress of the fluid (Fig. 3D). We estimate the externally imposed shear stress σ_{th} as the characteristic viscous stress of a lid-driven flow in a passive fluid with the same viscosity as the active fluid: $\sigma_{\text{th}} = \eta\,\dot{\gamma}$, where $\eta \approx 4.5$ mPa · s is the viscosity of the microtubule-kinesin active fluid[6,8] and $\dot{\gamma} \equiv \Delta v/\Delta r$ is the shear rate with Δv as the change in flow speed over the characteristic length scale Δr. At the critical thread speed of $v_{\text{th}} = 120$ μm/s, the thread induced a vortex whose edge, touching the thread, moved at 120 μm/s (no-slip boundary condition; Fig. S3A). From this edge to the center of the vortex, the flow speed decreased to zero over a distance of 360 μm (Fig. S3B), leading to a shear rate of $\dot{\gamma} \approx \frac{120\ \mu\text{m/s}}{360\ \mu\text{m}} = 0.33\ \text{s}^{-1}$ and a shear stress of $\sigma_{\text{th}} \approx 4.5\ \text{mPa} \cdot \text{s} \times 0.33\ \text{s}^{-1} = 1.5$ mPa on the active fluid. This represents the critical shear stress threshold above which the external shear stress dominates the active fluid's dynamics.

Similarly, we estimated the characteristic shear stress at the onset of flow reversal in the toroidal system (Fig. 5B), where the reversal rate λ becomes nonzero as the thread speed exceeded ~30 μm/s. In this case, the mini cavity flow formed near the moving thread (Fig. 4B, middle panel), indicating that external shear locally drives the flow. The distance from the thread surface to the vortex center is approximately half of the channel width (~250 μm). Using the same relation, $\sigma_{\text{th}} = \eta\,(\Delta v/\Delta r)$ with $\Delta v = 30$ μm/s and $\Delta r = 250$ μm, we obtained $\sigma_{\text{th}} \approx 0.5$ mPa. This stress value is comparable to the critical shear stress in the cuboidal system (~1.5 mPa), above which external shear dominates the active fluid dynamics.

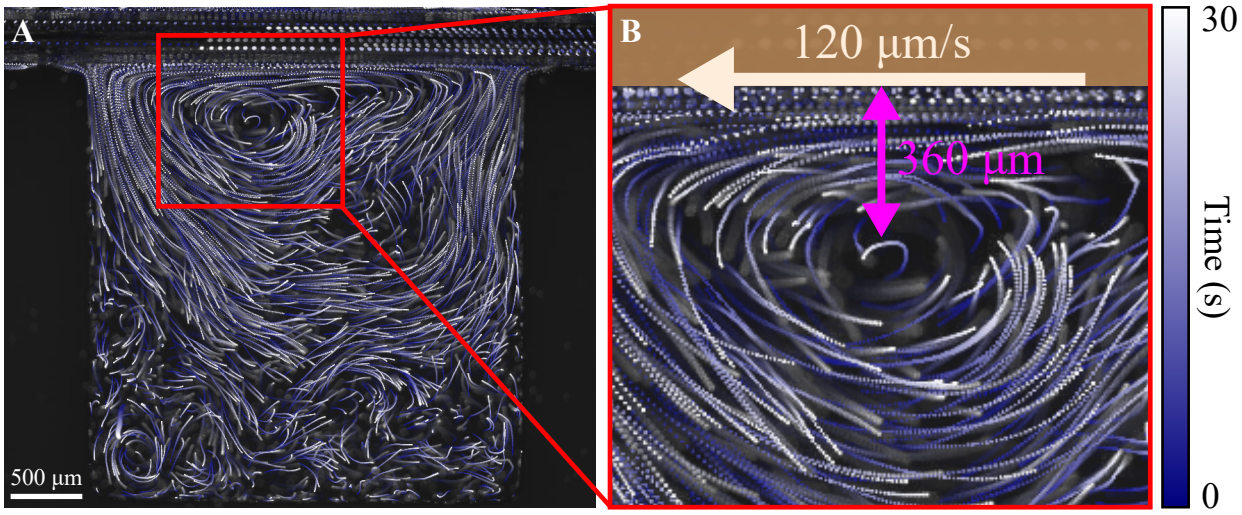

Fig. S3: Estimation of the critical external shear stress. (A) Composite image created by stacking 60 sequential tracer images of the active fluid confined in the thin cuboidal cavity with the thread motion of 120 μm/s. The colors represent a time lapse, transitioning from dark blue to white over 30 seconds (see colorbar in panel B). The composite image shows the formation of a cavity-wide vortex induced by the thread motion. (B) Close-up of the area near the thread (shaded brown) and vortex center from panel A. This close-up highlights the thread motion (120 μm/s), the vortex center (0 μm/s), and the distance from the thread surface to the vortex center (360 μm).

Section S3: Estimation of wall-friction (Brinkman) stress

In our thin cuboidal cavity system, the active fluid is confined between two parallel plates separated by a small gap h that is much smaller than the lateral dimension L ($h \ll L$; Hele-Shaw cell).[9] Under such confinement, the fluid experiences not only internal active stress and externally imposed shear stress, but also a hydrodynamic drag from the top and bottom plates. This effect can be captured by averaging the three-dimensional Stokes equation across the thin gap, yielding an effective two-dimensional description with an additional friction term, resembling the Brinkman equation in theory of porous media where the fluid flow experiences friction due to finite permeability of the media.[10–13] To derive this term, we start from the steady Stokes equation for an incompressible fluid of viscosity η:

$$\eta(\nabla_\perp^2 v_i + \partial_z^2 v_i) - \partial_i p = 0, \tag{S1}$$

with $\nabla_\perp^2 \equiv \partial_x^2 + \partial_y^2$ is the in-plane Laplacian. Since the system is shallow ($h \ll L$), incompressibility of the fluid ($\partial_x v_x + \partial_y v_y + \partial_z v_z = 0$) implies $v_z \sim \left(\frac{h}{L}\right) v_{x,y}$ so the vertical velocity is small compared with the in-plane components and can be neglected.

In addition, since the fluid is confined between two parallel plates separated by a small gap h, the no-slip boundary condition enforces that the velocity is zero at both the top and bottom plates. Under an in-plane pressure gradient, the viscous stress causes the velocity to increase from zero at one wall to a maximum at mid-height and then decreases back to zero at the opposite wall. The simplest function that satisfies these boundary conditions is a parabola, $v_{x,y} \propto z(h - z)$, which is a well-known Poiseuille profile for slow, laminar flow between parallel plates.[10] Therefore, the in-plane velocity can be written as

$$v_\alpha(x, y, z) = \bar{v}_\alpha(x, y)\phi(z), \tag{S2}$$

where $\alpha = x$ or y, $\phi(z) \propto z(h - z)$ and $\bar{v}_\alpha(x, y)$ is the depth-averaged in-plane velocity:

$$\bar{v}_\alpha(x, y) = \frac{1}{h}\int_0^h dz\ v_\alpha(x, y, z), \tag{S3}$$

which implies $\phi(z) = \frac{6}{h^2} z(h - z)$, satisfying the no-slip boundary conditions $\phi(0) = \phi(h) = 0$. Plugging Eq. S2 into Eq. S1, we obtain

$$\eta\phi(z)\nabla_\perp^2 \bar{v}_\alpha(x, y) + \eta\bar{v}_\alpha(x, y)\partial_z^2\phi(z) - \partial_\alpha p = 0. \tag{S4}$$

Multiplying both sides of Eq. S4 by $1/h$ and integrating from $z = 0$ to $z = h$ yields

$$\eta\nabla_\perp^2 \bar{v}_\alpha(x, y) - \eta\frac{12}{h^2}\bar{v}_\alpha(x, y) - \partial_\alpha \bar{p} = 0, \tag{S5}$$

where $\bar{p} \equiv \frac{1}{h}\int_0^h dz\ p$ is the depth-averaged pressure. This equation represents the depth-averaged Stokes equation, where the first term corresponds to in-plane viscous stress term, and the second term represents the additional friction arising from wall confinement, which resists the in-plane flow proportionally to the local velocity (the Brinkman term).[10–13] This term introduces a uniform hydrodynamic screening that slows the fluid dynamics without altering the overall flow structures.

To estimate the magnitude of this wall-friction stress, we note that the Brinkman term ($-\eta\frac{12}{h^2}\bar{v}_\alpha$) represents a body-force density. Multiplying by the gap height h converts it to an equivalent stress scale,

$$\sigma_B \sim -\frac{12\eta V}{h}, \tag{S6}$$

where V represents typical in-plane velocity of the confined fluid. In our case, $V \approx 10$ μm/s (Fig. 2A), $\eta = 4.5$ mPa · s,[6,8] and $h = 0.4$ mm. Together, we obtained $\sigma_B \approx 1$ mPa, which is comparable to the active stress scale of 1.5 mPa (Section S2). Because the Brinkman term represents a linear dissipative contribution that damps both active- and externally driven motion of fluid uniformly, its primary effect is to reduce the overall flow amplitude and alter the characteristic timescales. Therefore, it acts mainly as a hydrodynamic drag that moderates the fluid speed without introducing new flow structures (Fig. S4).

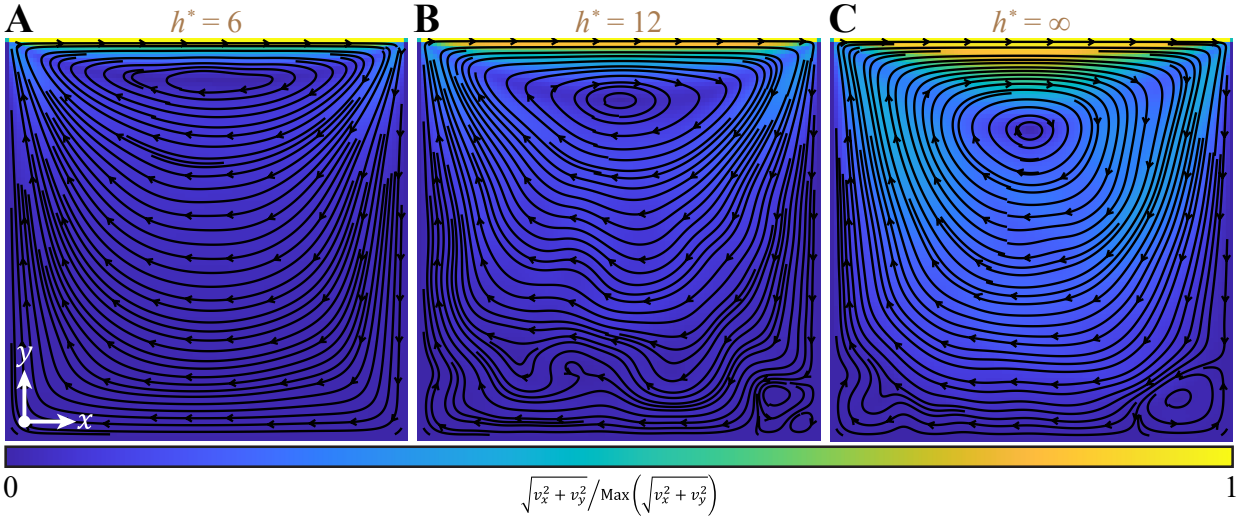

Fig. S4: Streamline plots overlaid with normalized flow speed colormaps for simulations incorporating the Brinkman term with different confinement heights. (A) $h^* = 6$. (B) $h^* = 12$. (C) $h^* = \infty$, equivalent to the 2D simulation without the Brinkman term. These simulations used the same driving conditions as in the right panel of Fig. 3A ($\Lambda = 1.8$); only the confinement height h^* was varied to tune the wall-friction contribution. The flow map demonstrates that the wall friction does not significantly alter the flow structure with minor shift of vortex center toward the moving boundary as the wall friction is enhanced (reducing h^*).

Section S4: Flow field subtraction between active and passive fluids

In our numerical model of the square cavity, the flow arises from a combination of internally generated active stress and externally imposed shear stress (Fig. 3). Therefore, it remains an open question how these two driving mechanisms interact—whether the resulting flow can be interpreted as a linear superposition of an active fluid flow without external forcing and a passive cavity flow, or whether external shear modifies the internal stress distribution in a nonlinear manner such that the two flows cannot be superimposed. To examine this coupling, we further analyzed the simulation data by computing the velocity field difference between active and passive (water) fluids subjected to identical boundary conditions (same lid speed, v_{th}). This analysis isolates the contribution of active stress from the total flow and reveals how the structure of the difference field evolves as the imposed shear stress increases (increasing Λ).

To perform this analysis, we used the simulated flow fields of the active fluid, $\boldsymbol{v}_a(t)$, and of the passive (water) fluid, $\boldsymbol{v}_w(t)$ under the same lid speed. After both systems reached a steady state, we computed the instantaneous velocity-difference field at corresponding time frames, $\Delta\boldsymbol{v}(t) \equiv \boldsymbol{v}_a(t) - \boldsymbol{v}_w(t)$. Our analysis revealed that in the absence of external shear (Λ = 0), the difference field corresponds to the intrinsic active fluid flow consisting of multiple small vortices driven by active stress (Fig. S5A). When a weak external shear is introduced (Λ = 0.05), the difference field begins to show the emergence of a larger central vortex while retaining smaller vortices throughout the cavity (Fig. S5B), comparable to the intrinsic vortices driven by active stress in the unforced state (Fig. S5A). This coexistence of the large and small vortices indicates that even weak external forcing can reorganize the active stress field, without suppressing its intrinsic vortices. When the external shear stress becomes comparable to the active stress (Λ = 0.9), the difference field becomes dominated by a cavity-wide vortex aligned with the direction of imposed shear (Fig. S5C). This evolution demonstrates that the externally applied shear modifies the active stress distribution, leading to cooperative flow structures rather than a linear superposition of active and passive components.[6,14,15]

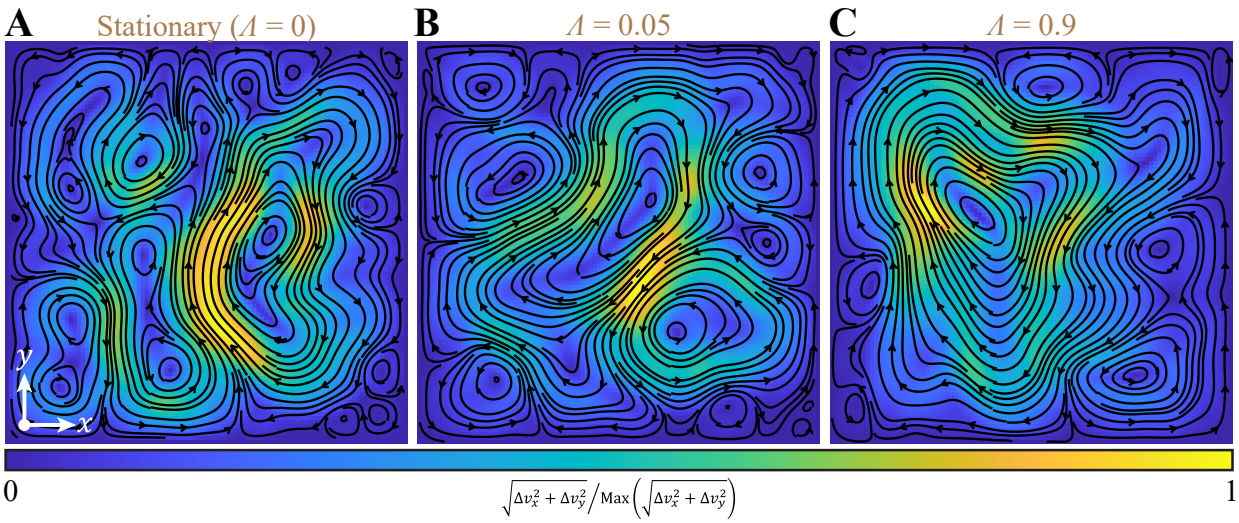

Fig. S5: Normalized velocity difference fields between active and passive (water) fluids at the same lid speed. (A) Λ = 0 (no external shear): intrinsic active fluid flow showing multiple small vortices driven by active stress. (B) Λ = 0.05: emergence of a larger central vortex while smaller intrinsic vortices persist throughout the cavity. (C) Λ = 0.9: a predominant cavity-wide vortex aligned with the direction of imposed shear, indicating reorganization of the active stress field under external forcing. Together, these results demonstrate that the flows of active and passive fluids cannot be linearly superimposed.

Together, these results demonstrate that the flow in the active fluid confined in a lid-driven cavity cannot be interpreted as a linear superposition of the intrinsic active fluid flow in the absence of driving and the passive cavity flow generated under the same driving conditions. The external shear modifies the nematic order and thereby alters the active stress distribution, such that the active and imposed shear stresses cannot be isolated as independent contributions within the active fluid system. This analysis highlights that the emergent flow structure of the active fluid confined in a lid-driven cavity arises from coupled interactions between active stress and externally imposed shear stress.

Section S5: Effect of external shear stress on microtubule network structure

The generation of extensile active stress in microtubule-kinesin active fluids depends on an intact microtubule network. If the network fragments under high shear stress, the ability to sustain active stress may be compromised, shifting the system's behavior toward passive fluid dynamics dominated by external shear forces.[6] To test whether the microtubule network fragments beyond the estimated critical shear stress of 1.5 mPa (Section S2), we used confocal microscopy to visualize the network structure under shear flow. If fragmentation were responsible for the observed transition, we could expect a loss of network connectivity at high shear stress.

To examine the structural response of the microtubule network to shear stress, we labeled microtubules with Alexa 647 (excitation: 650 nm; emission: 671 nm; Invitrogen, A-20006) following the previous protocol.[7,16,17] The microtubule-labeled active fluid sample was imaged by using a confocal microscope (Leica Microsystems, Stellaris 8) with a 10× objective (Leica Microsystems, 11506424, 10×, NA 0.4) and a white light laser tuned to 651 nm to excite Alexa 647–labeled microtubules; the resulting fluorescence was collected in the emission range of 654–775 nm. To observe the network structure in response to thread motion, we imaged the mid-plane of the sample near the top center of the cuboidal boundary, close to the thread (Fig. S6A). The network was imaged every second for one hour during which the thread first remained stationary for 10 minutes before it started to move continuously for 20 minutes after which it was stationary once more (Movie S4).

To analyze the network structure, we adopted the structure tensor package from DIPlib library (version 3.2) available on GitHub. This package was used to extract the microtubule orientations $\boldsymbol{u}$ in the confocal images; the microtubule orientations were determined by finding the direction perpendicular to the principal direction of the image's structure tensor $\nabla I \otimes \nabla I$ where I is the pixel value of the image (Fig. S6A).[18] Once the orientations $\boldsymbol{u}$ were extracted, we converted these vectors into angles θ representing the orientation direction with respect to the horizontal axis (Fig. S6B inset). To reveal how the orientation angles θ of microtubule bundles were influenced by the thread motion, we analyzed the probability density function of the orientation angles θ both for when the thread was stationary and when it moved at 134 ± 15 μm/s (Fig. S6B). This analysis showed that, while the bundles preferred to align parallel to the thread surface (0 degrees) when the thread was stationary (black curve), the thread motion further enhanced this alignment, resulting in a larger portion of bundles orienting around 0 degrees (red curve). This observation indicated that the thread motion enhanced bundle alignment.

To further characterize the spatial distribution of the degree of alignment, we analyzed the nematic order parameter S as a function of distance from the thread surface (Fig. S6C). To determine S, we collected the orientation vectors $\boldsymbol{u}$ of the microtubule bundles at the same distance from the thread and constructed the nematic order tensor $\boldsymbol{Q}(y)$ defined as $\boldsymbol{Q}(y) \equiv \langle 2\boldsymbol{u}(x,y,t) \otimes \boldsymbol{u}(x,y,t) - \boldsymbol{I} \rangle_{x,t}$ where $\boldsymbol{I}$ is the identity tensor and $\langle\ \rangle_{x,t}$ denoted the average over horizontal axis and time. The largest eigenvalue of the $\boldsymbol{Q}$ tensor determined the nematic order parameter S. Our analysis revealed that when the thread was stationary, the nematic order parameter rapidly decayed from the thread surface with a decay length scale of 70 μm (black curve) while this length scale was extended to 410 μm when the thread was in motion (red curve). This observation indicated that the thread motion thickened the nematic layer near the thread surface (where $S \geq 0.3$).

Despite these changes in alignment, our confocal data did not reveal the fragmentation of the microtubule network when subjected to an external shear stress exceeding the critical threshold of 1.5 mPa (Movie S4). This lack of observed fragmentation falsifies our hypothesis that the network would break down under high shear stress ($\gtrsim$1.5 mPa) and stands in contrast to the findings of Gagnon *et al.*, whose confocal and

rheological data suggested network breakage above a critical external stress of ~2 mPa.[6] The discrepancy may arise from differences in confinement geometry, which likely influence whether shear stress leads to microtubule network rupture. Nonetheless, our confocal data indicated that the structural breakdown does not account for the observed transition. Instead, we propose an alternative hypothesis that the kinematic transition observed in our active fluid's flow behavior arose primarily from the competition between internal active stress and external shear stress, rather than from network rupture.

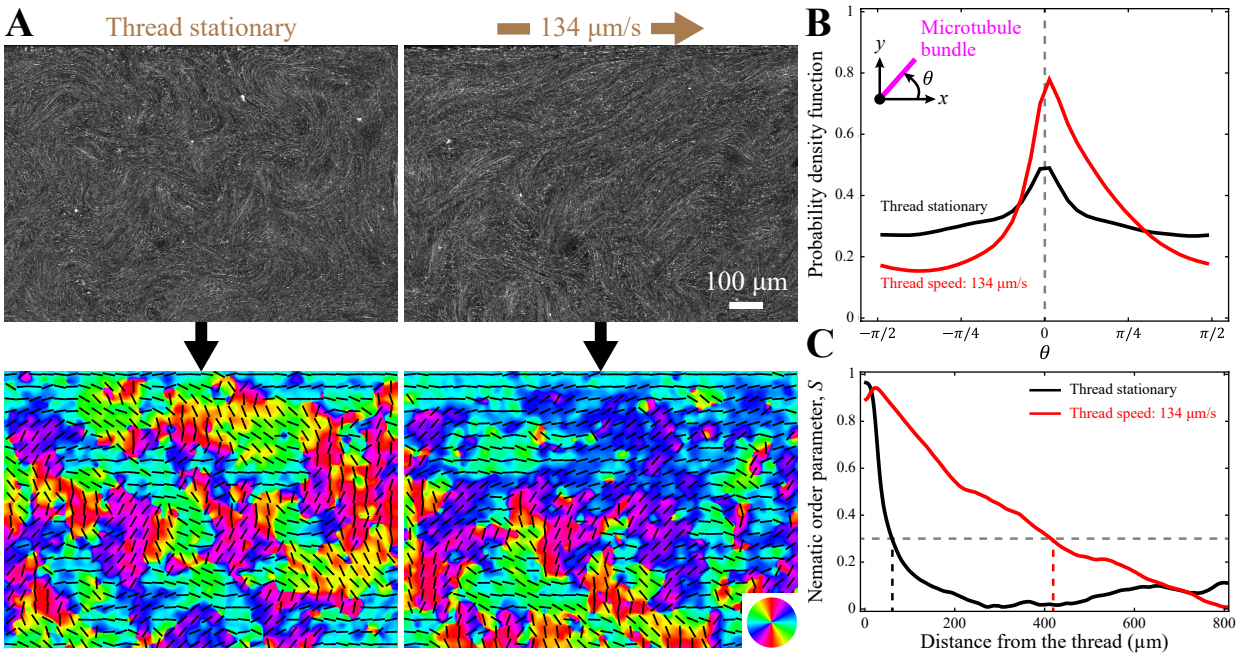

Fig. S6: Orientational order in the active fluid. (A) Confocal microscopy images of the microtubule network near the center of the thread and in the mid-plane of the chamber (top row). The bottom row shows corresponding orientational distribution colormaps with blue-green tones for horizontal orientations, red-yellow tones for vertical orientations, and black line segments indicating the director field (see also Movie S4). Note the greater alignment of the microtubules with the thread when the thread is moving. (B) Probability density functions of orientation distribution for the cases of zero thread speed and an intermediate thread speed (134 ± 15 μm/s). When the thread was stationary (black curve), the orientation exhibited a peak at zero degrees; away from the peak, the distribution decayed symmetrically, suggesting that the bundles were not strictly constrained to horizontal orientation and could equally orient in clockwise or counterclockwise directions. (C) Nematic order parameter S vs. distance from the thread. When the thread was stationary (black curve), the nematic order parameter quickly decayed, with a decay length scale of ~70 μm (vertical dashed black line determined by the intersection of the black curve and the horizontal gray dashed line representing the criterion of $S = 0.3$ for the nematic state). When the thread was moving (red curve), the nematic order parameter decayed with a decay length scale of ~410 μm (vertical red dashed line).

.

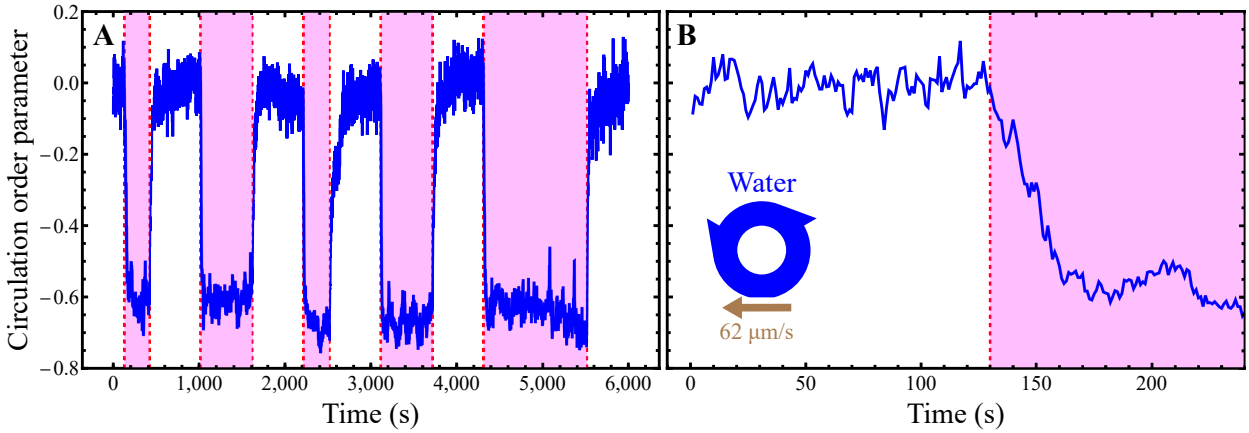

Fig. S7: Response of water/heavy water mixture confined in a ratcheted toroid to the thread motion. (A) Evolution of the circulation order parameter of a water/heavy water mixture confined in a toroid. The outer boundary was decorated with two teeth (panel B inset). The mixture was driven by the thread motion as in Fig. 4A. The mixture was driven intermittently by the thread at a speed of 62 ± 14 μm/s, with driving phases ranging from 5 to 20 minutes (shaded areas) and intervening rest phases of 10 minutes. The driving decreased the circulation order parameter from 0 to -0.6. Once the driving stopped, the flow of water was dissipated by the internal viscous stress and boundary-induced friction, causing the water to become quiescent, and the circulation order parameter returned to 0. (B) Close-up view of panel A, illustrating the rapid thread-induced drop of circulation order parameter from 0 to -0.6 within 30 seconds, with a reversal rate of $\lambda \approx 1.2$ min^{-1}, which contrasted with the active fluid case where the reversal rate at the comparable thread speed was much lower ($\lambda \approx 0.2$ min^{-1}; Fig. 5B). This difference highlights the active fluid's inherent resistance to circulation direction reversal under external driving.

Movie S1: Response of the active fluid to external driving in a thin cuboid. The active fluid was confined in a thin cuboid (3 mm × 3 mm × 0.4 mm) with one side replaced by a moving thread. When the thread moved at 8 μm/s (left panel), the active fluid developed turbulence-like chaotic flow whose flow pattern was minimally influenced by the thread motion, behaving similarly to an isolated active fluid in which the internal active stress dominated the flow dynamics. When the thread speed was increased to 58 μm/s (middle panel), the active fluid maintained its chaotic flow pattern in the area far away from the thread (bottom half of the cavity), whereas a cavity-wide vortex intermittently formed near the thread, indicating a regime where both internal active stress and external driving comparably influenced the flow. When the thread speed was further increased to 430 μm/s (right panel), the chaotic motion of the active fluid was inhibited; a cavity-wide vortex formed, demonstrating an external driving-dominated regime. The time stamp indicates hour:minute:second.

Movie S2: Response of passive water to external driving in a thin cuboid. The passive water/heavy water mixture was confined in a thin cuboid, similar to the active fluid system in Movie S1, but lacking internal active stress and remaining stationary without external force. When the thread moved at 120 μm/s (left panel), the mixture formed a single cavity-wide vortex. At a higher thread speed of 290 μm/s, a similar vortex pattern was observed but with an increased spinning speed (middle panel). At 460 μm/s, the vortex spun even faster while maintaining a similar flow pattern. These consistent flow patterns across different thread speeds demonstrates that at low Reynolds numbers ($\mathrm{Re} = 0.3$–1), the flow patterns of passive water/heavy water mixture remained invariant while the spinning speed scaled with the driving speed.[19] Additionally, this flow pattern resembled the vortex observed in the active fluid system at a thread speed of 430 μm/s (right panel in Movie S1), reinforcing that the flow pattern was primarily driven by external forces with negligible contribution from internal active stress. The time stamp indicates hour:minute:second.

Movie S3: Response of fuel-deprived inactive gel to external driving in a thin cuboid. The fuel-deprived inactive gel was confined in a thin cuboidal boundary, similar to the active fluid system in Movie S1, but without ATP, thus rendering the system inactive. Unlike passive water, this system consisted of a microtubule network crosslinked by immobile motor dimers (due to the lack of ATP), forming a viscoelastic network. At a low thread speed of 80 μm/s (left panel), the network remained nearly stationary with minor jiggling, exhibiting the elastic response of the network. When the thread speed increased to 210 μm/s (middle panel), the top portion near the thread became mobile and fluidized, while the bottom portion remained stationary. The fluidized portion contained chunks moving together as a group, indicating partial fluidization with areas retaining their structures. These chunks were no longer observed when the thread moved at 520 μm/s (right panel); the top portion was fully fluidized, forming a single vortex, whereas the bottom half remained stationary. This result highlights the viscoelastic response of the fuel-deprived inactive gel to varying external driving speeds, transitioning from a gel-like to a fluid-like phase. The time stamp indicates hour:minute:second.

Movie S4: Response of the microtubule network to external driving in a thin cuboid. The microtubule-kinesin active fluid was confined in a thin cuboid similar to the setup in Movie S1, but with the imaging capturing microtubules instead of tracers. To highlight the influence of thread motion on the microtubule network, we imaged the network on the top center part of the thin cuboidal boundary near the thread. When the thread was stationary (0 μm/s, left panel), the microtubule network exhibited chaotic, turbulence-like flow, with microtubule bundles continuously extending, buckling, and annealing.[7] When the thread moved at an average speed of 134 ± 15 μm/s (right panel), the microtubules near the thread aligned along the direction of the thread movement, forming a thin nematic layer. This observation indicated that external driving transitioned the network from a chaotic structure to an ordered nematic state. The time stamp indicates hour:minute:second.

Movie S5: Evolution of the simulated flow field in a 2D extensile active fluid confined in a square cavity ($L^* = 45$) from $t = 0$ to 40. This movie corresponds to Fig. 3A, showing how the flow evolves

under different externally imposed shear stresses. Left: Lid stationary ($\Lambda = 0$), where the flow exhibits chaotic, turbulence-like flow. Middle: Moderate shear stress ($\Lambda = 0.38$), where chaotic flow coexists with shear-driven flow. Right: High shear stress ($\Lambda = 1.8$), where chaotic flow is suppressed, and the flow adopts a cavity flow-like pattern. The colormap represents the flow speed normalized by its maximum value in each panel.

Movie S6: Response of the active fluid to external driving in a toroid decorated with two ratchet teeth. The active fluid was confined in a toroid (outer radius 1,000 μm, inner radius 500 μm, height 400 μm) with a segment of the outer boundary replaced by a moving thread. The outer boundary was decorated with two ratchet teeth to direct the spontaneously developed coherent flow of the active fluid in the counterclockwise direction due to internal active stress, based on previous studies.[20] Initially, when the thread was stationary, the active fluid established a coherent counterclockwise flow. When the thread began to move at 50 μm/s in the opposite direction (00:15:40), it caused the fluid flow to shift to clockwise in response to the thread-induced external driving force (00:17:30). The thread continued to move for 20 minutes before stopping (00:35:30). After the thread stopped, the active fluid maintained its clockwise flow for 10 minutes before spontaneously reverting to its natural counterclockwise flowing state (00:50:30), demonstrating its ability to return to its inherent flow pattern once the external influence was removed. The time stamp indicates hour:minute:second.

Movie S7: Response of the active fluid to external driving in a toroid decorated with three ratchet teeth. Similar to the setup in Movie S6, the active fluid was confined in a toroid and initially developed a counterclockwise coherent flow before the thread started to move. However, in this setup, the outer boundary was decorated with three ratchet teeth, and the thread was driven at 210 μm/s. When the thread began to move (00:26:00), the fluid flow direction shifted to clockwise in response to the thread-induced external driving force. The thread continued to move for 20 minutes before stopping (00:46:00). After the thread stopped, the active fluid maintained its clockwise flow for 8.5 minutes before spontaneously reverting to its natural counterclockwise state (00:54:30). This result demonstrated the consistent response of the active fluid upon external driving force across different confinement geometries (2 teeth vs. 3 teeth), showing its ability to revert to its natural coherent flow state even at a higher thread speed (210 μm/s) than in Movie S6 (50 μm/s). The time stamp indicates hour:minute:second.

Movie S8: Response of the active fluid to low-speed external driving in a toroid decorated with one ratchet tooth. Similar to the setup in Movies S6 and S7, the active fluid was confined in a toroid, initially developing a counterclockwise coherent flow before the thread started to move. However, in this setup, the outer boundary was decorated with only one ratchet tooth, and the thread was driven at 40 μm/s. When the thread began to move (00:31:00), the fluid flow direction shifted to clockwise in response to the thread-induced external driving force. The thread continued to move for 20 minutes before stopping (00:51:00). After the thread stopped, the active fluid maintained its clockwise flow for 12 minutes before spontaneously reverting to its natural counterclockwise state (01:02:40). This result demonstrates that the active fluid was capable of reverting to its natural coherent flow state even when the outer boundary contained only one tooth. The time stamp indicates hour:minute:second.

Movie S9: Response of the active fluid to high-speed external driving in a toroid decorated with one ratchet tooth. Similar to the setup in Movie S8, the active fluid was confined in a toroid with 1 tooth, but with a higher driving speed of 130 μm/s. Initially, the active fluid developed a spontaneous counterclockwise coherent flow. When the thread started to move (00:25:30), the fluid flow direction shifted to clockwise in response to the thread-induced external driving. Unlike the observations with 2 and 3 teeth, where the active fluid consistently reverted to its natural state after being driven (Movies S6 and S7), the active fluid confined in the one-tooth toroid maintained its clockwise flow after the thread stopped moving (00:45:30) and continued in this direction for the remainder of the observation (until 01:55:00). This result indicates that the ability of the active fluid to revert to its natural counterclockwise state is influenced by both the number of ratchet teeth and the driving speed. While lower driving speeds (40 μm/s)

allowed the fluid to revert (Movie S8), higher speeds (130 μm/s) prevented this reversion. The time stamp indicates hour:minute:second.

Movie S10: Response of the active fluid to external driving in connected toroids. The active fluid was confined in a connected toroidal geometry consisting of two laterally overlapping toroids (each toroid had the same inner/outer radii, channel width, and height as in Movie S6; the channels overlapped by 10%). The upper toroid was directly driven by the translating thread, whereas the lower toroid contained three ratchet teeth that biased clockwise circulation. Before driving, the lower toroid exhibited spontaneous clockwise circulation and induced counterclockwise flow in the upper toroid. The system remained in this counter-rotating state for ~50 minutes, until the thread began to move (00:48:29) at a speed of 120 ± 12 μm/s. After driving began, the upper toroid reversed circulation almost immediately (00:52:20), whereas the lower toroid reversed more gradually (01:10:35). The driving lasted for ~50 minutes before the thread stopped moving (01:36:23). Following the cessation of driving, both toroids remained in this counter-rotating state for ~1.5 hours, until the lower toroid reverted to clockwise (03:06:07), followed by the upper toroid returning to counterclockwise (03:39:52). This experiment demonstrated the cooperative interaction between external shear stress and internal active stress, allowing the influence of external driving to propagate across the connected geometry into the second (lower) toroid. The time stamp indicates hour:minute:second.

Movie S11: Response of the passive fluid to external driving in connected toroids. The passive water/heavy water mixture was confined in the same connected toroidal geometry as in Movie S10, except that this passive fluid system lacked internal active stresses and remained stationary in the absence of external forcing. When the thread was moving at a speed of 136 ± 10 μm/s, only the upper toroid developed clockwise circulation, whereas the lower toroid remained nearly quiescent. This control experiment demonstrated that without the cooperation of internal active stresses, the influence of external driving was limited to the upper toroid and did not transmit into the second toroid. The time stamp indicates hour:minute:second.

References

1 L. Giomi, Geometry and topology of turbulence in active nematics, *Phys Rev X*, 2015, **5**, 031003.

2 R. Benzi, S. Patarnello and P. Santangelo, Self-similar coherent structures in two-dimensional decaying turbulence, *Journal of Physics A: Mathematical and General*, 1988, **21**, 1221.

3 J. Weiss, The dynamics of enstrophy transfer in two-dimensional hydrodynamics, *Physica D: Nonlinear Phenomena*, 1991, **48**, 273–294.

4 B. Najma, W.-S. Wei, A. Baskaran, P. J. Foster and G. Duclos, Microscopic interactions control a structural transition in active mixtures of microtubules and molecular motors, *Proc Natl Acad Sci U S A*, 2024, **121**, e2300174121.

5 B. Najma, M. Varghese, L. Tsidilkovski, L. Lemma, A. Baskaran and G. Duclos, Competing instabilities reveal how to rationally design and control active crosslinked gels, *Nat Commun*, 2022, **13**, 6465.

6 D. A. Gagnon, C. Dessi, J. P. Berezney, R. Boros, D. T. N. Chen, Z. Dogic and D. L. Blair, Shear-induced gelation of self-yielding active networks, *Phys Rev Lett*, 2020, **125**, 178003.

7 T. Sanchez, D. T. N. Chen, S. J. DeCamp, M. Heymann and Z. Dogic, Spontaneous motion in hierarchically assembled active matter, *Nature*, 2012, **491**, 431–434.

8 T. E. Bate, M. E. Varney, E. H. Taylor, J. H. Dickie, C.-C. Chueh, M. M. Norton and K.-T. Wu, Self-mixing in microtubule-kinesin active fluid from nonuniform to uniform distribution of activity, *Nat Commun*, 2022, **13**, 6573.

9 X. Wang, B. Klaasen, J. Degrève, A. Mahulkar, G. Heynderickx, M.-F. Reyniers, B. Blanpain and F. Verhaeghe, Volume-of-fluid simulations of bubble dynamics in a vertical Hele-Shaw cell, *Phys Fluids*, 2016, **28**, 053304.

10 D. J. Acheson, *Elementary fluid dynamics*, Clarendon Press : Oxford University Press, Oxford, 2009.

11 H. C. Brinkman, A calculation of the viscous force exerted by a flowing fluid on a dense swarm of particles, *Appl. Sci. Res.*, 1949, **1**, 27–34.

12 Y. Almoteri and E. Lushi, Microswimmer collective dynamics in Brinkman flows, *Physical Review Fluids*, 2025, **10**, 083102.

13 H. Liu, P. R. Patil and U. Narusawa, On Darcy-Brinkman equation: viscous flow between two parallel plates packed with regular square arrays of cylinders, *Entropy*, 2007, **9**, 118–131.

14 H. M. López, J. Gachelin, C. Douarche, H. Auradou and E. Clément, Turning bacteria suspensions into superfluids, *Phys Rev Lett*, 2015, **115**, 028301.

15 A. Sokolov and I. S. Aranson, Reduction of viscosity in suspension of swimming bacteria, *Phys Rev Lett*, 2009, **103**, 148101.

16 T. E. Bate, E. J. Jarvis, M. E. Varney and K.-T. Wu, Controlling flow speeds of microtubule-based 3D active fluids using temperature, *J Vis Exp*, 2019, e60484.

17 G. Henkin, S. J. DeCamp, D. T. N. Chen, T. Sanchez and Z. Dogic, Tunable dynamics of microtubule-based active isotropic gels, *Philos Trans A Math Phys Eng Sci*, 2014, **372**, 20140142.

18 A. Opathalage, M. M. Norton, M. P. N. Juniper, B. Langeslay, S. A. Aghvami, S. Fraden and Z. Dogic, Self-organized dynamics and the transition to turbulence of confined active nematics, *Proc Natl Acad Sci U S A*, 2019, **116**, 4788–4797.

19 S. Sen, S. Mittal and G. Biswas, Steady separated flow past a circular cylinder at low Reynolds numbers, *Journal of Fluid Mechanics*, 2009, **620**, 89–119.

20 K.-T. Wu, J. B. Hishamunda, D. T. N. Chen, S. J. DeCamp, Y.-W. Chang, A. Fernández-Nieves, S. Fraden and Z. Dogic, Transition from turbulent to coherent flows in confined three-dimensional active fluids, *Science*, 2017, **355**, eaal1979.